Higher-order topological superconductivity in type-II time-reversal-symmetric Weyl semimetals with a hybrid pairing

Junkang Huang^{1,2}, Z. D. Wang^{1,2,3,4},* and Tao Zhou^{1,2†}

¹Guangdong Basic Research Center of Excellence for Structure and Fundamental Interactions of Matter,
Guangdong Provincial Key Laboratory of Quantum Engineering and Quantum Materials,
School of Physics, South China Normal University, Guangzhou 510006, China

²Guangdong-Hong Kong Joint Laboratory of Quantum Matter,
Frontier Research Institute for Physics, South China Normal University, Guangzhou 510006, China

³HK Institute of Quantum Science & Technology,
The University of Hong Kong, Pokfulam Road, Hong Kong, China

⁴Hong Kong Branch for Quantum Science Center of Guangdong-Hong
Kong-Macau Great Bay Area, 3 Binlang Road, Shenzhen, China

We employed the self-consistent method on a two-orbital type-II time-reversal-symmetric Weyl semimetal, revealing a hybrid pairing of singlet s-wave and triplet p-wave. We present a detailed analysis of the normal-state electronic structure and the self-consistent results. Our findings indicate that the selection of hybrid pairings is governed by distinct surface Fermi-arc configurations: specifically, s-wave pairing dominates on the bottom surface, while p-wave pairing prevails on the top. Furthermore, the emergent superconducting state is a second-order topological superconductors with hinge states in the system. Our results identify type-II time-reversal-invariant Weyl semimetals as a promising intrinsic platform for realizing unconventional and topological superconductivity.

I. INTRODUCTION

Superconductivity in topologically non-trivial materials represents one of the most compelling frontiers in condensed matter physics, where the interplay between exotic electronic structures and quantum phenomena gives rise to exotic physical properties. Among these systems, Weyl semimetals (WSM) have emerged as particularly intriguing candidates, characterized by their paired Weyl nodes and topological Fermi arc. The fundamental question driving current research is whether these unique electronic configurations and nontrivial topological properties can induce unconventional or topological superconductivity—a question that has motivated numerous experimental investigations in the past [1–7].

Time-reversal-symmetric (TR) WSM represent a more promising platform for superconductivity compared with their TR-breaking counterparts, since superconductivity is suppressed by the breaking of TR. This advantage has led to the discovery of superconductivity in numerous TRWSM have been reported to exhibit the signature of superconductivity, such as type-I TRWSM like PtBi₂ [8–10], NbX (X = As,P) [11, 12], TaX (X = As,P) [13–15], and type-II TRWSM including MoTe₂ [16, 17], WTe₂ [18, 19] and TalrTe₄ [20, 21].

The exotic electronic structure of TRWSM, particularly the surface-localized Fermi arcs, has been shown to play a crucial role in their superconducting behavior. Previously, edge supercurrents have been detected in MoTe₂ [22]. When proximized to a conventional s-wave superconductor, the observed supercurrent indicates an

incompatibility between the intrinsic superconductivity and the conventional superconductivity. These two findings imply the possible existence of intrinsic unconventional topological superconductivity in MoTe₂ [23]. Additionally, muon-spin relaxation and rotation (μ SR) experiments have revealed an unconventional superconducting pairing order in T_d -MoTe₂ [24].

More compelling evidence for unconventional superconductivity emerges in $PtBi_2$ compounds. Recent angle-resolved photoemission spectroscopy (ARPES) experiments on $PtBi_2$ compounds have provided direct evidence for superconducting Fermi arcs and revealed an anisotropic superconducting gap structure, strongly suggesting unconventional pairing mechanisms [25, 26]. Complementary STM measurements have quantified the superconducting gaps of approximately 20 meV in t-PtBi₂ [27, 28] and 0.5 meV in γ -PtBi₂ [29], respectively. Theoretical studies on superconductivity in TRWSM mostly concentrate on surface superconductivity in type-I systems [30–34], topological properties [35–40], and Andreev reflection phenomena at normal-superconductor interfaces [41].

In the past several years, the emergence of secondorder topological three-dimensional superconductors have attracted considerable interest, characterized by hinge states. Such systems have been theoretically proposed to be realized through chiral superconducting pairing [42, 43] or via heterostructures composed of topological insulators and conventional superconductors [44, 45]. Recent theoretical work has suggested that PtBi₂ may exhibit chiral superconductivity accompanied by hinge states [26]. Type-II TRWSM possess tilted Weyl cones along with numerous Fermi arcs facilitating the formation of large Fermi surface [46], which is conducive to superconductivity that may further give rise to unconventional topological superconductivity. However, theo-

^{*} zwang@hku.hk

[†] tzhou@scnu.edu.cn

(3)

retical investigations into this promising platform remain relatively limited.

In our paper, a two-orbital tight-binding model is presented to describe the type-II TRWSM. The electronic structure has been meticulously studied. We employ the self-consistent method to obtain the superconductingstate ground state. The resulting pairing in our model is a hybrid pairing of singlet s-wave and triplet p-wave pairings. The system's large zero-energy density of states and abundant surface Fermi arcs enable this superconducting phase to emerge with relatively weak pairing potentials compared to time-reversal-breaking or type-I TR system [33, 47]. The resulting bulk superconductor is fully gapped and possesses non-trivial second-order topological hinge states. This higher-order character is confirmed by the local electronic structure and quadrupole moment. Our work intends to provide new insights into unconventional and topological superconductivity in the type-II TRWSM.

The remainder of this paper is organized as follows: Section II presents the model and the formalism; Section III discusses the numerical results; and Section IV provides a summary.

II. MODEL AND FORMALISM

We consider a minimal Hamiltonian for TRWSM expressed as follows:

$$H = \sum_{\mathbf{k}\tau\sigma} (\gamma \cos 2k_x \cos k_y) c_{\mathbf{k}\tau\sigma}^{\dagger} c_{\mathbf{k}\tau\sigma} + \sum_{\mathbf{k}\sigma} [(M - 2t_x \cos k_x) - 2t_y \cos 2k_y - 2t_z \cos \mathbf{k_z}) (c_{\mathbf{k}\tau\sigma}^{\dagger} c_{\mathbf{k}\tau'\sigma} + c_{\mathbf{k}\tau'\sigma}^{\dagger} c_{\mathbf{k}\tau\sigma})$$

$$+2\lambda_y \cos k_y (c_{\mathbf{k}\tau\sigma}^{\dagger} c_{\mathbf{k}\tau\sigma} - c_{\mathbf{k}\tau'\sigma}^{\dagger} c_{\mathbf{k}\tau'\sigma})$$

$$+2\lambda_z \sin \mathbf{k_z} (-ic_{\mathbf{k}\tau\sigma}^{\dagger} c_{\mathbf{k}\tau'\sigma} + ic_{\mathbf{k}\tau'\sigma}^{\dagger} c_{\mathbf{k}\tau\sigma})] + H_I, \qquad (1)$$

where τ/τ' and σ denote the orbital and spin indices, respectively. M denotes the onsite interorbital coupling constant. t_x, t_y, t_z and λ_z represent the offsite interorbital coupling constants. λ_y signifies the intraorbital hopping constant. Notably, both λ_u and λ_z are responsible for inducing the non-trivial topological properties of system. The transition from type-I to typle-II WSM is governed by the long-range intraorbital constant γ . This model hosts two pairs of Weyl points located at $(\pm \pi/2, \pm \pi/2, 0)$. For $|\gamma| < 0.5$, the system behaves as a type-I Weyl semimetal, characterized by a Fermi surface comprising only the four Weyl nodes. When $|\gamma| > 0.5$, it transitions into a type-II Weyl semimetal. At this time, where the emergence of electron and hole Fermi pockets leads to an extended Fermi surface. H_I is the nearest neighbor intraorbital attractive exchange interaction term, which accounts for the superconducting pairing, being given by:

$$H_I = -V \sum_{i\alpha} n_{i,\tau\uparrow} n_{i+\alpha,\tau\downarrow}.$$
 (2)

Here, $n_{i,\tau\uparrow}$ represents the particle number operator, and $n_{i,\tau\uparrow} = c_{i,\tau\uparrow}^{\dagger} c_{i,\tau\uparrow}$. The mean-field order parameters can be defined as $\Delta_{\tau\alpha} = V \langle c_{i,\tau\uparrow} c_{i+\alpha,\tau\downarrow} \rangle$, where α denotes the six nearest neighbor vectors. V represents the superconducting pairing strength.

For our model, the Fermi arcs are localized in the surfaces of the system and can be exuded by opening the boundary in the z direction. In this partial opening boundary condition, the Hamiltonian can be expressed as $H = \sum_{z,\mathbf{k}} \Psi_{z,\mathbf{k}}^{\dagger} \hat{M}_z(\mathbf{k}) \Psi_{z,\mathbf{k}}$, where \hat{M}_z is a $2N_z \times 2N_z$ matrix and the Nambu vector $\Psi_{z,\mathbf{k}} = (u_{z,\mathbf{k}\tau}, v_{z,\mathbf{k}\tau})^T$. $u_{z,\mathbf{k}\tau} = (c_{z,\mathbf{k}1\uparrow}.c_{z,\mathbf{k}2\uparrow})$ and $v_{z,\mathbf{k}\tau} = \left(c_{z,-\mathbf{k}1\downarrow}^{\dagger}, c_{z,-\mathbf{k}2\downarrow}^{\dagger}\right)$. Here the indices 1 and 2 denote the orbitals. z/z' is the layer index.

The superconducting pairing orders are not independent and should be determined by the other parameters in the model. In our paper, the order parameters are obtained by self-consistent calculation. The self-consistent equations are expressed as:

$$\Delta_{\tau\alpha'}^{z} = \frac{V}{2N_{1}} \sum_{\mathbf{k}\tau n} u_{z,\mathbf{k}\tau n} v_{z,\mathbf{k}\tau n}^{*} \tanh\left(\frac{\beta E_{\mathbf{k}n}}{2}\right) \exp\left(-i\mathbf{k} \cdot \alpha'\right),$$

 $\Delta_{\tau}^{z,z'} = \frac{V}{2N_1} \sum_{\mathbf{k} = n} u_{z,\mathbf{k}\tau n} v_{z',\mathbf{k}\tau n}^* \tanh\left(\frac{\beta E_{\mathbf{k}n}}{2}\right),\tag{4}$

where α' denotes the four in-plane nearest-neighbor vectors \hat{x} , \hat{y} , $-\hat{x}$ and $-\hat{y}$. $\Delta^z_{\tau\alpha'}$ is the intralayer pairing order parameter in the z layer. $\Delta^{z,z'}_{\tau}$ is the interlayer pairing order parameter from z to z' layers (|z-z'|=1). N_1 is the number of unit cells in k_x - k_y momentum space.

The spectral function of layer z and orbital τ can be calculated by:

(1)
$$A_{\tau}^{z}(k_{x}, k_{y}, \omega) = -\frac{1}{\pi} \sum_{n} \operatorname{Im} \frac{|u_{2z+\tau-2, n}(k_{x}, k_{y})|^{2}}{\omega - E_{n}(k_{x}, k_{y}) + i\Gamma}, \quad (5)$$

The orbital index $\tau=1$ and $\tau=2$ denote the orbital 1 and 2, respectively. The eigenvector $u_{2z+\tau-2,n}(k_x,k_y)$ and eigenvalue $E_n(k_x,k_y)$ are obtained by diagonalizing the Hamiltonian with the partially opening boundary condition in the z direction. Γ is a damping factor being set as $\Gamma=0.01$.

The local density of states (LDOS) of layer z and orbital τ can be expressed by integrating the spectral function $A_{\tau}^{z}(k_{x},k_{y},\omega)$ over the entire k_{x} - k_{y} momentum space:

$$\rho_{\tau}^{z}\left(\omega\right) = \frac{1}{N_{1}} \sum_{k_{x}, k_{y}} A_{\tau}^{z}\left(k_{x}, k_{y}, \omega\right). \tag{6}$$

To explore the hinge states in the system, we have considered the Hamiltonian with the partially opening boundary condition in the x and z direction. In this boundary condition, the Hamiltonian is given by H=

$$\sum_{xz,k_{y}} \Psi_{xz,k_{y}}^{\dagger} \hat{M}_{xz} \left(\mathbf{k_{y}}\right) \Psi_{xz,k_{y}}. \ \hat{M}_{xz} \text{ is a } 2N_{x}N_{z} \times 2N_{x}N_{z}$$

The τ -orbital spectral function at site (x, z) is expressed as:

$$A_{\tau}^{(x,z)}(k_{y},\omega) = -\frac{1}{\pi} \sum_{n} \operatorname{Im} \frac{|u_{2N_{x}z+2x+\tau-2N_{x}-2,n}(k_{y})|^{2}}{\omega - E_{n}(k_{y}) + i\Gamma},$$
(7)

For the three-dimensional system, we can define the quadrupole moment $q_{xz}\left(k_{y}\right)$ in x-z plane for each k_{y} -sliced layer [43]. The quadrupole moment $q_{xz}\left(k_{y}\right)$ can be expressed as:

$$q_{xz}(k_y) = \frac{1}{2\pi} \operatorname{Im} \log \left[\operatorname{Det} \left(\Phi_{k_y}^{\dagger} Q \Phi_{k_y} \right) \sqrt{\operatorname{Det} (Q^{\dagger})} \right]. \tag{8}$$

Here Φ_{k_y} is a $2N_xN_z \times N_xN_z$ matrix, which is constructed by columnwise packing the occupied eigenstates with $\Phi_{k_y} = (u_{1,k_y}, u_{2,k_y}, ..., u_{N_xN_z,k_y})$. The matrix Q is a $2N_xN_z \times 2N_xN_z$ diagonal constant matrix. The diagonal elements are defined as $e^{2\pi ixz/N_xN_z}$.

In the following presented results, unless otherwise specified, the input parameters are set as $M=1,\ t_x=t_z=\lambda_y=\lambda_z=1,\ t_y=0.5,\ \gamma=1,\ N_x=N_z=50$ and the pairing strength V=2.

III. RESULTS AND DISCUSSION

A. Normal-state electronic structure

We begin by presenting the normal-state electronic structure. Fig. 1 summarises the bulk and surface energy spectra with the partially opening boundary condition in the z direction. The energy spectrum for $k_y = 0.5\pi$ slice is shown in Fig. 1(a). The double-degenerate Fermi arcs with bold red lines match two Weyl points $(\pm \pi/2, \pi/2)$ carrying opposite chirality. At the k_x direction, the Weyl cones are not tilted by γ term. The energy spectrum for $k_x = 0.5\pi$ slice is represented in Fig. 1(b). The oblique edge bands with bold red lines intersect at the locations of two Wevl points. Each tilted Wevl cone generates an electron pocket and a hole pocket at the two sides of the Weyl points. The electron and hole pockets are connected by the Weyl points. The tilted Weyl cones form large Fermi surface inducing numerous zero-energy electronic states, which contrasts to conventional Type-I WSM. Time-reversal-symmetry, large Fermi surface and numerous zero-energy electronic states are beneficial to the superconductivity.

The zero-energy spectral functions on the two surfaces of the WSM (A^1 and A^{N_z}) are exhibited in Figs. 1(c) and 1(d), where A^z represents the spectral function for the both two orbital channels, as $A^z = A_1^z + A_2^z$. On both surfaces, the horizontal and vertical Fermi arcs contribute most of zero-energy states, while the zero-energy states

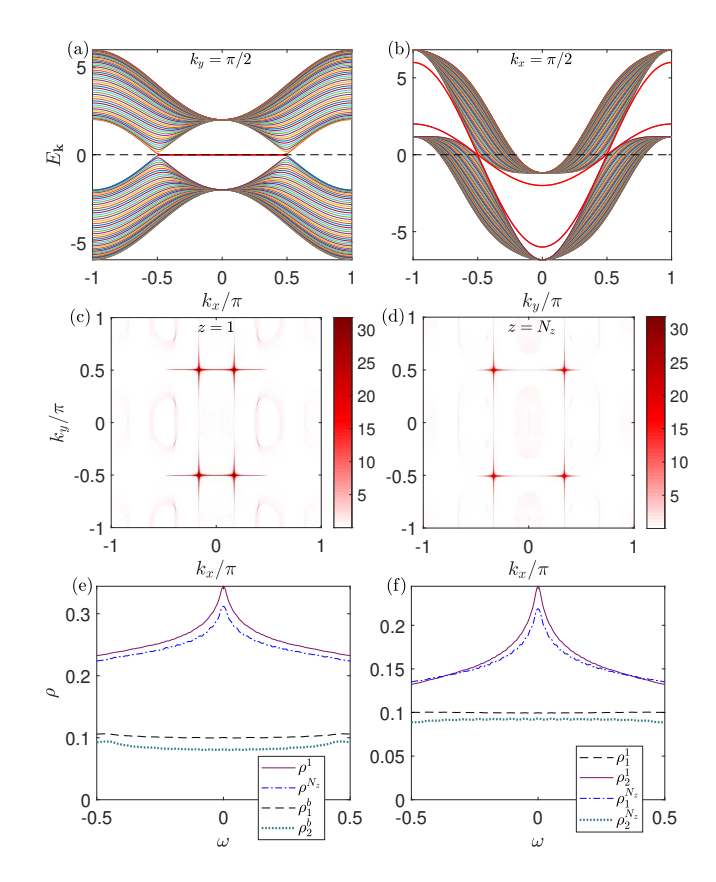


FIG. 1. Normal-state electronic structures with partially opening boundary condition in the z direction. Top row: energy spectra at the $k_y=\pi/2$ slice (a), and at the $k_x=\pi/2$ slice (b). Middle row: zero-energy spectral functions on the z=1 surface (c) and on the $z=N_z$ surface (d). Bottom row: orbital-resolved LDOS curves on the z=1, $z=N_z$ surfaces and in the bulk ($z=N_z/2$).

projected by the bulk are much weaker. Due to the broken inversion symmetry, the locations of Fermi arcs on the two surfaces are different. On the z=1 surface, as shown in Fig. 1(c), each shorter $k_y = \pm 0.5\pi$ horizontal Fermi arc connect two Weyl points. The longer vertical Fermi arcs intersect with the shorter ones at points $(\pm 0.16\pi, \pm 0.5\pi)$. The longer Fermi arcs do not connect Weyl points and stretch across the Brillouin zone in the k_y direction. Furthermore, the two longer Fermi arcs are very close together. On the $z = N_z$ surface, presented in Fig. 1(d), the $k_y=\pm 0.5\pi$ horizontal Fermi arcs are shorter and connect two Weyl points, while $k_x = \pm 0.33\pi$ vertical Fermi arcs are longer and stretch across the Brillouin zone. Compared with the longer vertical Fermi arcs on the z=1 surface, the vertical ones on the $z=N_z$ surface are separated far away.

The contribution of Fermi arcs can be unveiled by the LDOS curves, showcased in Figs. 1(e) and 1(f). ρ^1 and ρ^{N_z} without subscript signify $\rho^z = \rho_1^z + \rho_2^z$. In Fig. 1(e), the Fermi arcs induce a sharp zero-energy peak localized on the surface z=1 (solid crimson line) and surface $z=N_z$ (blue dash-dotted line). The bulk LDOS for

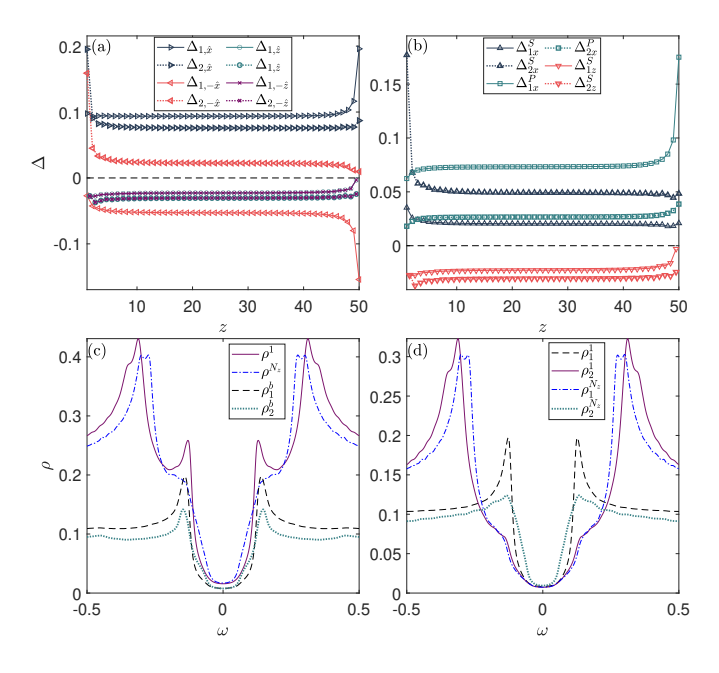


FIG. 2. Superconducting pairing and superconducting-state electronic structure with partially opening boundary condition in the z direction. Top row: the layer-dependent superconducting order parameters obtained by the self-consistent method. Bottom row: orbital-resolved superconducting-state LDOS curves on the $z=1,\ z=N_z$ surfaces, and in the bulk $(z=N_z/2)$.

orbitals 1 and 2 is weaker and flatter at low-energy level. From Figs. 1(e) and 1(f), it is found that the orbital 2 dominates the localized sharp zero-energy peaks on the z=1 surface, while orbital 1 dominates the sharp peaks on the $z=N_z$ surface, due to the inversion symmetry being broken. In Fig. 1(f), LDOS for orbital 1 on the surface z=1 is plotted as a black dashed line, and that for orbital 2 on the surface $z=N_z$ with a green dotted line are weak and almost projected by the bulk LDOS.

B. Hybrid pairing in the superconducting state

Fig. 2 presents self-consistently determined superconducting pairing and the resulting LDOS spectra in the superconducting state with partially opening boundary condition in the z direction. Utilizing the self-consistent method in EQs.[4,5], the superconducting pairing order parameters at each layer can be obtained. In Fig. 2(a), the order parameters are large at the edge, then quickly decrease to constants from the edge into the bulk, owing to numerous zero-energy electronic states contributed by Fermi arcs localized in the surfaces. Both $\Delta_{1,\hat{z}} = \Delta_{1,-\hat{z}}$ and $\Delta_{2,\hat{z}} = \Delta_{2,-\hat{z}}$ in each layer indicate only singlet pairings in the z direction, while $\Delta_{1,\hat{x}} \neq \pm \Delta_{1,-\hat{x}}$ and $\Delta_{2,\hat{x}} \neq \pm \Delta_{2,-\hat{x}}$ imply that both singlet and triplet pairings emerge in the x direction. In the y direction, the order parameters are small and neglected here.

To be clear, these order parameters can be modi-

fied into the familiar s-wave, p-wave forms. We obtain the extended s-wave order parameters as $\Delta_{\tau x}^S(z) = \left(\Delta_{\tau,\hat{x}}^z + \Delta_{\tau,-\hat{x}}^z\right)/2$, and $\Delta_{\tau z}^S(z,z') = \left(\Delta_{\tau}^{z,z'} + \Delta_{\tau}^{z',z}\right)/2$. The triplet p_x -wave order parameters can be obtained by $\Delta_{\tau x}^P(z) = \left(\Delta_{\tau,\hat{x}}^z - \Delta_{\tau,-\hat{x}}^z\right)/2$. Then the s-wave and p-wave form order parameters are depicted in Fig. 2(b). In Fig. 2(b), the intralayer s-wave order parameter for orbital 2 $\left(\Delta_{2x}^S\right)$ is dominant on the z=1 surface, while p_x -wave order parameter for orbital 1 $\left(\Delta_{1x}^P\right)$ is dominant on the $z=N_z$ surface, due to the different normal-state electron structures on these two surfaces mentioned in Fig. 1. Besides, the intralayer s-wave order parameter for orbital 1 $\left(\Delta_{1x}^S\right)$, p_x -wave order parameter for orbital 2 $\left(\Delta_{2x}^S\right)$ and interlayer s-wave order parameters $\left(\Delta_{\tau z}^S\right)$ for both two orbitals are weaker and almost maintain a small range both in bulk and surfaces.

The LDOS curves of the superconducting states are shown in Figs.2(c) and 2(d). All the LDOS curves near zero energy are ∪-shaped, revealing the system is fully gapped in the superconducting states. In Fig. 2(c), the bulk LDOS has a single smaller superconducting gap, while the surface LDOS possesses a two-gap feature. For surface LDOS, the higher superconducting coherent peaks, corresponding to the larger gap, are induced by the superconducting Fermi arcs. The location of the smaller superconducting gap nearly overlaps with that in the bulk LDOS, because the smaller gap is the projection of that in the bulk. In Fig. 2(d), for the z = 1 surface, the larger gap is dominated by orbital 2 and the smaller gap is the projection of the bulk mainly for orbital 1. Conversely, on the $z = N_z$ surface, the larger and smaller gaps are dominated by orbital 1 and 2, respectively.

Spatial distinction of the pairing order on the opposite surfaces is rooted in the different Fermi-arc geometries. In the k_x - k_y plane, extended s-wave pairing varies as $\cos k_x$ or $\cos k_y$ vanishes at $k_x = \pm \pi/2$ or $k_y = \pm \pi/2$, whereas triplet p-wave pairing varies as $\sin k_x$ or $\sin k_y$ is maximal there. Both in the two surfaces, the horizontal Fermi arcs are localized at $k_y = \pm 0.5\pi$, resulting in the weakness of s_y -wave pairing. The z=1 surface hosts vertical Fermi arcs near $k_x = 0$ line, which stabilize a dominant s_x -wave pairing with a secondary p_x wave component. The opposite situation occurs on the $z = N_z$ surface, where vertical arcs near $k_y = \pm \pi/2$ line lead to a predominant p_x -wave pairing with a subsidiary s_x -wave component. The hybrid pairing of s_x - and p_x wave can make the maximal gap at the position of the vertical Fermi arcs and fully gap the system.

Moreover, the p_y component of triplet pairing is absent. On a square lattice p_x and p_y pairing usually coexist and can combine into a time-reversal-breaking p_x+ip_y (p+ip-wave) state that strongly competes with singlet pairing. In our model, however, the C_4 symmetry is absent and the Fermi surface passes through (0,0) and $(\pm \pi, \pm \pi)$ —the nodal points of a p+ip gap—so a pure p+ip state would leave the system gapless and cannot be the thermodynamic ground state; self-consistent cal-

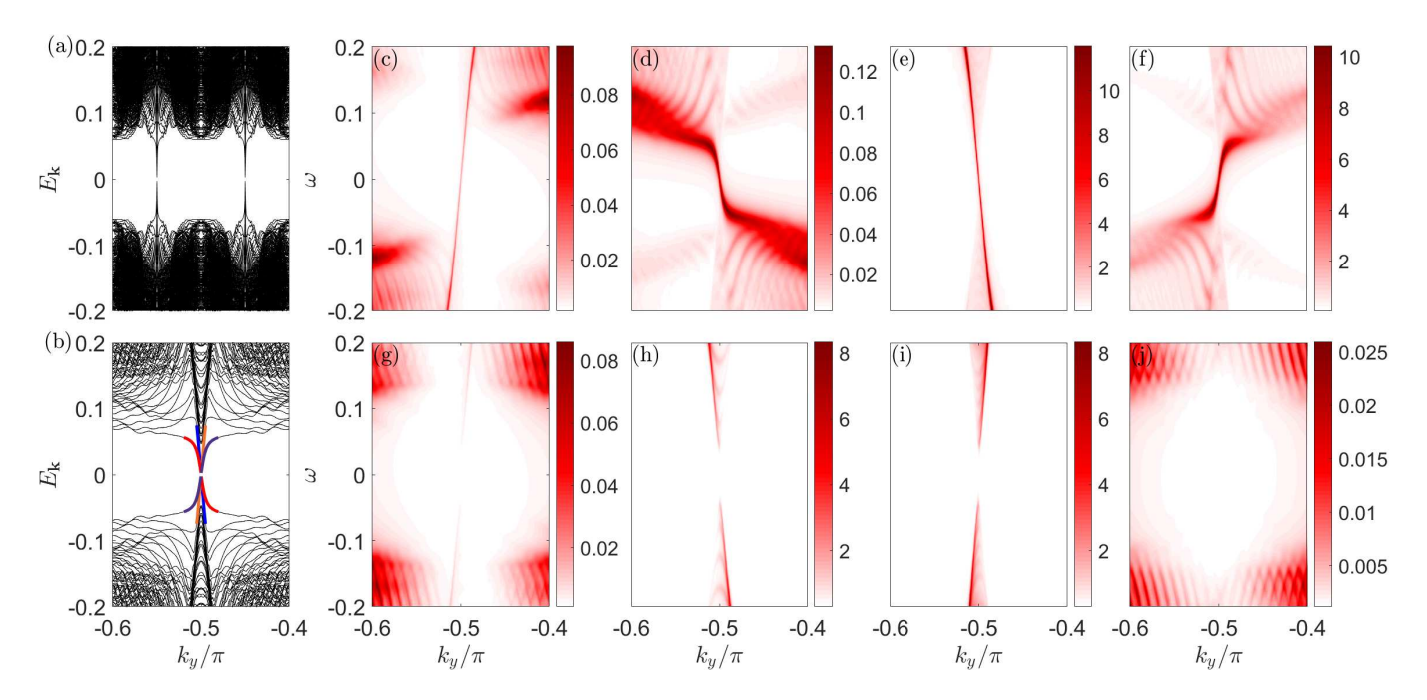


FIG. 3. Electronic structures with partially opening boundary condition in the x and z directions. In the left panel, (a) superconducting spectrum; (b) zoom-in of the region of the left edge bands. In the right panel, orbital dependent spectral functions at the four corners (c-f) and at the lateral edges (g-j).

culations confirm that this channel is never favored. As illustrated in Fig. 1, the normal-state Fermi arcs are predominantly $k_x = \text{constant}$ lines that traverse the entire Brillouin zone, whereas $k_y = \text{constant}$ arcs are short and fragmentary; this anisotropy stabilizes p_x and s_x pairing over p_y and s_y pairing.

Thus, in TRWSM systems, the geometry of Fermi surface, formed by Fermi arcs localized on the surfaces, is one of significant factors in determining the preferred superconducting pairing symmetry. Searching for or engineering TRWSM with specific Fermi-arcs configurations presents a viable pathway to achieve unconventional superconductivity in these materials.

C. Topological properties

To interrogate the second-order topology of the superconducting phase we impose partially opening boundaries condition in both x and z directions. The electronic structures with this boundary condition are shown in Fig. 3. The energy band is presented in Fig. 3(a), and is symmetric about $k_y = 0$. For clarity, the enlarged view for the left edge bands is shown in Fig. 3(b). In Figs. 3(a) and 3(b), the bulk energy band is fully gapped, and the edge bands are represented by the coloured lines, which intersect at $k_y = \pm \pi/2$. This indicates the non-trivial second-order topology in the system.

The spectral functions at four corner sites are exhibited in Figs. 3(c)-3(f). In these figures, the ascending edge band with the orange line can be identified by spectral

function $A_1^{(1,1)}$, as shown in Fig. 3(c). The descending edge band with the red line can be recognized by spectral function $A_2^{(1,N_z)}$, being presented in Fig. 3(d). The spectral functions for both orbitals are notably weak since orbital 1 and orbital 2 have minimal weight on the z=1 and $z=N_z$ surfaces, respectively.

The descending edge band with the blue line and the ascending edge band with the purple line can be well identified by spectral function $A_2^{(N_x,1)}$ [Fig. 3(e)] and $A_1^{(N_x,N_z)}$ [Fig. 3(f)], respectively. The last two spectral functions are much larger than the first two. These spectral functions for the four corner edge bands reveal that the mirror symmetry in x-z plane has been broken in the superconducting states. The proportion of the four edge states is in extreme disequilibrium.

Figs. 3(g)-3(j) depict the spectral functions at the middle of the z=1 and $z=N_z$ surfaces. In Figs. 3(g) and 3(h), the spectral functions $A_1^{(N_x/2,1)}$ and $A_2^{(N_x/2,1)}$ are shown, while the spectral functions $A_1^{(N_x/2,N_z)}$ and $A_2^{(N_x/2,N_z)}$ are presented in Figs. 3(i) and 3(j). All these four spectral functions reveal that the Fermi arcs have been fully gapped by the hybrid superconducting pairing and the topological edge states are only localized at the four hinges.

To confirm the higher-order topology further we compute the quadrupole moment $q_{xz}(k_y)$ [Eq.(8)]. The quadrupole moment $q_{xz}(k_y)$ for each k_y -sliced layer can be utilized to describe the non-trivial second-order topology in the system. The curve of quadrupole moment is shown in Fig. 4. Time-reversal symmetry enforces

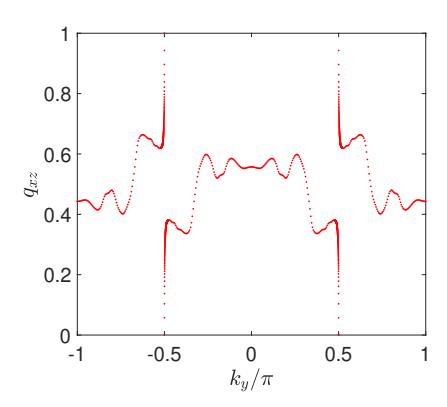


FIG. 4. Quadrupole moment for each k_y -sliced layer.

 $q_{xz}\left(k_y\right)=q_{xz}\left(-k_y\right)$. In Fig. 4, the quadrupole moment has quite sudden changes and makes windings at $k_y=\pm\pi/2$, indicating the non-trivial second-order topology of the system. The windings of quadrupole moment at $k_y=\pm\pi/2$ are relevant to the edge-band crossings at $k_y=\pm\pi/2$. Besides, the windings of quadrupole moment at $k_y=-\pi/2$ and $k_y=\pi/2$ are in the opposite direction, implying that the hinge states here are not chiral and without any current passing through in our system and TR breaking.

Our study positions type-II TRWSM as a programmable laboratory for on-demand unconventional superconductivity. Multiple momentum-resolved Fermi arcs coexist on each surface, their distinct orbital textures and connectivities acting as built-in selectors that stabilize singlet or triplet pairing on opposite surfaces without external interfaces or proximity effects. Additionally, type-II TRWSM dispersion carves out an extended Fermi surface that hosts a large density of states at the Fermi level; the profusion of zero-energy carriers cooperatively amplifies the pairing instability and points toward a realistic route to push the critical temperature of topological superconductivity well beyond the ceilings of type-I or TR-breaking counterparts.

Notably, the positions of Weyl points and their associated Fermi arcs can be reconfigured through surface decoration [48], pressure [49], or strain [50]. This tunability

positions type-II TRWSMs as a versatile single-material arena, where high- T_c unconventional superconductivity, nontrivial topology, and other emergent quantum states can be generated, controlled, and hybridized. Such a system provides an exceptional setting for exploring novel and hybrid quantum phases.

IV. SUMMARY

In summary, we have employed a minimal model for type-II TRWSM. In this system, a large Fermi surface is formed by bulk electron and hole pockets, complemented by the Fermi arcs localized on the surfaces. The Fermi pockets supply mainly bulk zero-energy electronic states, while the Fermi arcs induce a pronounced zeroenergy peak in the LDOS on the surfaces. Through the self-consistent calculation, a mixed s-wave and p-wave pairing is revealed and coexists both in bulk and on the surfaces. A spatial dichotomy has been examined: swave pairing is dominant on one surface, whereas the p-wave pairing is prominent on the other surface. This distinct pairing mechanism stems from the differing patterns of Fermi arcs on the two surfaces. In WSM, various Fermi-arc configurations may induce an intrinsic unconventional topological superconductivity in the system.

In the superconducting states of our model, mirror-symmetry-breaking hinge states emerge and are dominated by different orbital channels. We have provided numerical evidences for energy bands, spectral functions in the four hinges. Furthermore, the second-order topological property is also corroborated by the windings of quadrupole moment at certain momenta, which is directly linked to the edge-band crossing at these specific momenta. Our findings suggest that type-II TRWSM be a promising platform for exploring unconventional and topological superconductivity.

ACKNOWLEDGMENTS

This work was supported by Guangdong Provincial Quantum Science Strategic Initiative (Grant No. GDZX2404001), the NSFC/RGC JRS grant (N_HKU 774/21), and GRF of Hong Kong (17303/23).

^[1] A. Veyrat, V. Labracherie, D. L. Bashlakov, F. Caglieris, J. I. Facio, G. Shipunov, T. Charvin, R. Acharya, Y. Naidyuk, R. Giraud, J. Van Den Brink, B. Büchner, C. Hess, S. Aswartham, and J. Dufouleur, Berezinskii– Kosterlitz-Thouless Transition in the Type-I Weyl Semimetal PtBi₂, Nano Lett. 23, 1229 (2023).

^[2] W. Cao, N. Zhao, C. Pei, Q. Wang, Q. Zhang, T. Ying, Y. Zhao, L. Gao, C. Li, N. Yu, L. Gu, Y. Chen, K. Liu, and Y. Qi, Pressure-induced superconductivity in the noncentrosymmetric Weyl semimetals LaAlX (X = Si,

Ge), Phys. Rev. B 105, 174502 (2022).

^[3] Z. Wang, J. Olivares, H. Namiki, V. Pareek, K. Dani, T. Sasagawa, V. Madhavan, and Y. Okada, Visualizing superconductivity in a doped Weyl semimetal with broken inversion symmetry, Phys. Rev. B 104, 115102 (2021).

^[4] J. Wang, X. Chen, Y. Zhou, C. An, Y. Zhou, C. Gu, M. Tian, and Z. Yang, Pressure-induced superconductivity in trigonal layered PtBi₂ with triply degenerate point fermions, Phys. Rev. B 103, 014507 (2021).

- [5] E. Emmanouilidou, S. Mardanya, J. Xing, P. V. S. Reddy, A. Agarwal, T.-R. Chang, and N. Ni, Fermiology and type-I superconductivity in the chiral superconductor NbGe₂ with Kramers-Weyl fermions, Phys. Rev. B 102, 235144 (2020).
- [6] D. Tang, Y. Chen, M. Yang, Q. Wang, Y. Zou, X. Wang, Z. Li, C. Yi, Y. Shi, X. Kong, G. Song, Y. Xu, X. Wei, M. Weinert, L. Li, W. Fang, and Y. Liu, Strong-coupling anisotropic s-wave superconductivity in the type-II Weyl semimetal TaIrTe₄, Phys. Rev. B 103, 174508 (2021).
- [7] T. Shang, S. K. Ghosh, M. Smidman, D. J. Gawryluk, C. Baines, A. Wang, W. Xie, Y. Chen, M. O. Ajeesh, M. Nicklas, E. Pomjakushina, M. Medarde, M. Shi, J. F. Annett, H. Yuan, J. Quintanilla, and T. Shiroka, Spintriplet superconductivity in Weyl nodal-line semimetals, npj Quantum Mater. 7, 35 (2022).
- [8] A. Kuibarov, S. Changdar, R. Vocaturo, O. Su-A. Fedorov, R. Lou, Μ. Krivenkov, vorov. Harnagea, S. Wurmehl, J. van den Brink, В. Büchner, and S. Borisenko, Three prerequisites for high-temperature superconductivity (2025), arXiv:2509.02178 [cond-mat].
- [9] G. Shipunov, I. Kovalchuk, B. R. Piening, V. Labracherie, A. Veyrat, D. Wolf, A. Lubk, S. Subakti, R. Giraud, J. Dufouleur, S. Shokri, F. Caglieris, C. Hess, D. V. Efremov, B. Büchner, and S. Aswartham, Polymorphic PtBi₂: Growth, structure, and superconducting properties, Phys. Rev. Mater. 4, 124202 (2020).
- [10] J. Zabala, V. F. Correa, F. J. Castro, and P. Pedrazzini, Enhanced weak superconductivity in trigonal γ-PtBi₂, Journal of Physics: Condensed Matter 36, 285701 (2024).
- [11] M. D. Bachmann, N. Nair, F. Flicker, R. Ilan, T. Meng, N. J. Ghimire, E. D. Bauer, F. Ronning, J. G. Analytis, and P. J. W. Moll, Inducing superconductivity in Weyl semimetal microstructures by selective ion sputtering, Sci. Adv. 3, e1602983 (2017).
- [12] W. Deng, J. Zhen, Q. Huang, Y. Wang, H. Dong, S. Wan, S. Zhang, J. Feng, and B. Chen, Pressurequenched superconductivity in weyl semimetal NbP induced by electronic phase transitions under pressure, J. Phys. Chem. Lett. 13, 5514 (2022).
- [13] H. Wang, H. Wang, Y. Chen, J. Luo, Z. Yuan, J. Liu, Y. Wang, S. Jia, X.-J. Liu, J. Wei, and J. Wang, Discovery of tip induced unconventional superconductivity on weyl semimetal, Sci. Bull. 62, 425 (2017).
- [14] X.-Y. Hou, Y.-D. Gu, S.-J. Li, L.-X. Zhao, W.-L. Zhu, Z. Wang, M.-D. Zhang, F. Zhang, L. Zhang, H. Zi, Y.-W. Wu, H.-X. Yang, Z.-A. Ren, P. Zhang, G.-F. Chen, N. Hao, and L. Shan, Two superconducting phases induced at point contacts on the Weyl semimetal TaAs, Phys. Rev. B 101, 134503 (2020).
- [15] J. Luo, Y. Li, J. Li, T. Hashimoto, T. Kawakami, H. Lu, S. Jia, M. Sato, and J. Wang, Surface superconductivity on Weyl semimetal induced by nonmagnetic and ferromagnetic tips, Phys. Rev. Materials 3, 124201 (2019).
- [16] Y. Qi, P. G. Naumov, M. N. Ali, C. R. Rajamathi, W. Schnelle, O. Barkalov, M. Hanfland, S.-C. Wu, C. Shekhar, Y. Sun, V. Süß, M. Schmidt, U. Schwarz, E. Pippel, P. Werner, R. Hillebrand, T. Förster, E. Kampert, S. Parkin, R. J. Cava, C. Felser, B. Yan, and S. A. Medvedev, Superconductivity in weyl semimetal candidate MoTe₂, Nat. Commun. 7, 11038 (2016).
- [17] F. C. Chen, X. Luo, R. C. Xiao, W. J. Lu, B. Zhang, H. X. Yang, J. Q. Li, Q. L. Pei, D. F. Shao, R. R. Zhang,

- L. S. Ling, C. Y. Xi, W. H. Song, and Y. P. Sun, Superconductivity enhancement in the S-doped weyl semimetal candidate MoTe₂, Appl. Phys. Lett. **108**, 162601 (2016).
- [18] X.-C. Pan, X. Chen, H. Liu, Y. Feng, Z. Wei, Y. Zhou, Z. Chi, L. Pi, F. Yen, F. Song, X. Wan, Z. Yang, B. Wang, G. Wang, and Y. Zhang, Pressure-driven dome-shaped superconductivity and electronic structural evolution in tungsten ditelluride, Nat. Commun. 6, 7805 (2015).
- [19] D. Kang, Y. Zhou, W. Yi, C. Yang, J. Guo, Y. Shi, S. Zhang, Z. Wang, C. Zhang, S. Jiang, A. Li, K. Yang, Q. Wu, G. Zhang, L. Sun, and Z. Zhao, Superconductivity emerging from a suppressed large magnetoresistant state in tungsten ditelluride, Nat. Commun. 6, 7804 (2015).
- [20] Y. Xing, Z. Shao, J. Ge, J. Luo, J. Wang, Z. Zhu, J. Liu, Y. Wang, Z. Zhao, J. Yan, D. Mandrus, B. Yan, X.-J. Liu, M. Pan, and J. Wang, Surface superconductivity in the type II weyl semimetal TaIrTe₄, Natl. Sci. Rev. 7, 579 (2020).
- [21] S. Cai, E. Emmanouilidou, J. Guo, X. Li, Y. Li, K. Yang, in t-PABLi, Q. Wu, N. Ni, and L. Sun, Observation of superconductivity in the pressurized weyl-semimetal candidate TaIrTe₄, Phys. Rev. B 99, 20503 (2019).
- [22] W. Wang, S. Kim, M. Liu, F. A. Cevallos, R. J. Cava, and N. P. Ong, Evidence for an edge supercurrent in the Weyl superconductor MoTe₂, Science 368, 534 (2020).
- [23] S. Kim, S. Lei, L. M. Schoop, R. J. Cava, and N. P. Ong, Edge supercurrent reveals competition between condensates in a Weyl superconductor, Nat. Phys. 20, 261 (2024).
- [24] Z. Guguchia, F. Von Rohr, Z. Shermadini, A. T. Lee, S. Banerjee, A. R. Wieteska, C. A. Marianetti, B. A. Frandsen, H. Luetkens, Z. Gong, S. C. Cheung, C. Baines, A. Shengelaya, G. Taniashvili, A. N. Pasupathy, E. Morenzoni, S. J. L. Billinge, A. Amato, R. J. Cava, R. Khasanov, and Y. J. Uemura, Signatures of the topological s± superconducting order parameter in the type-II Weyl semimetal Td-MoTe₂, Nat. Commun. 8, 1082 (2017).
- [25] A. Kuibarov, O. Suvorov, R. Vocaturo, A. Fedorov, R. Lou, L. Merkwitz, V. Voroshnin, J. I. Facio, K. Koepernik, A. Yaresko, G. Shipunov, S. Aswartham, J. V. D. Brink, B. Büchner, and S. Borisenko, Evidence of superconducting fermi arcs, Nature 626, 294 (2024).
- [26] S. Changdar, O. Suvorov, A. Kuibarov, S. Thirupathaiah, G. Shipunov, S. Aswartham, S. Wurmehl, I. Kovalchuk, K. Koepernik, C. Timm, B. Büchner, I. C. Fulga, S. Borisenko, and J. van den Brink, Topological nodal i-wave superconductivity in PtBi₂ (2025), arXiv:2507.01774 [cond-mat].
- [27] S. Schimmel, Y. Fasano, S. Hoffmann, J. Besproswanny, L. T. Corredor Bohorquez, J. Puig, B.-C. Elshalem, B. Kalisky, G. Shipunov, D. Baumann, S. Aswartham, B. Büchner, and C. Hess, Surface superconductivity in the topological weyl semimetal t-PtBi₂, Nat. Commun. 15, 9895 (2024).
- [28] X. Huang, L. Zhao, S. Schimmel, J. Besproswanny, P. Härtl, C. Hess, B. Büchner, and M. Bode, Sizable superconducting gap and anisotropic chiral topological super (2025), arXiv:2507.13843 [cond-mat].
- [29] J. A. Moreno, P. G. Talavera, E. Herrera, S. L. Valle, Z. Li, L.-L. Wang, S. Bud'ko, A. I. Buzdin, I. Guillamón, P. C. Canfield, and H. Suderow, Robust surface superconductivity and vortex lattice in the weyl sem.

- (2025), arXiv:2508.04867 [cond-mat].
- [30] H. Waje, F. Jakubczyk, J. van den Brink, and C. Timm, Ginzburg-landau theory for unconventional surface supercon [42] thirty Kin al ABi2 Higher-order topological insulators and (2025), arXiv:2507.02415 [cond-mat].
- [31] M. Trama, V. Könye, I. C. Fulga, and J. Van Den Brink, Self-consistent surface superconductivity in time-reversal symmetric weyl semimetals, Phys. Rev. B 112, 64514 (2025).
- [32] R. Vocaturo, K. Koepernik, J. I. Facio, C. Timm, I. C. Fulga, O. Janson, and J. Van Den Brink, Electronic structure of the surface-superconducting Weyl semimetal PtBi₂, Phys. Rev. B **110**, 054504 (2024).
- [33] X. Bai, W. LiMing, and T. Zhou, Superconductivity in weyl semimetals with time reversal symmetry, New J. Phys. **27**, 13003 (2025).
- [34] A. Nomani and P. Hosur, Intrinsic surface superconducting instability in type-I Weyl semimetals, Phys. Rev. B **108**, 165144 (2023).
- [35] R. Giwa and P. Hosur, Superconductor Vortex Spectrum Including Fermi Arc States in Time-Reversal Symmetric Weyl Semimetals, Phys. Rev. Lett. **130**, 156402 (2023).
- [36] R. Giwa and P. Hosur, Fermi Arc Criterion Surface Majorana Modes in Superconduct-Time-Reversal Symmetric Weyl Semimetals, Phys. Rev. Lett. 127, 187002 (2021).
- [37] R.-X. Zhang, Y.-T. Hsu, and S. Das Sarma, Dirac Higher-order topological superconductors, Phys. Rev. B 102, 094503 (2020).
- [38] Z. Yan, Z. Wu, and W. Huang, Vortex End Majorana Zero Modes in Superconducting Dirac and Weyl Semimetals, Phys. Rev. Lett. 124, 257001 (2020).
- [39] G. A. Hamilton, M. J. Park, and M. J. Gilbert, Topological d-wave superconductivity and nodal line-arc intersections in Wevl semimetals. Phys. Rev. B **100**, 134512 (2019).
- [40] P. Hosur, X. Dai, Z. Fang, and X.-L. Qi, Time-reversalinvariant topological superconductivity in doped Weyl semimetals, Phys. Rev. B 90, 045130 (2014).
- [41] A. Azizi and B. Abdollahipour, Andreev reflection at the interface of a normal Weyl semimetal

- and a superconducting type-II Weyl semimetal, Phys. Rev. B **102**, 024512 (2020).
- superconductors protected by inversion symmetry, Phys. Rev. B 97, 205136 (2018).
- [43] B. Fu, Z.-A. Hu, C.-A. Li, J. Li, and S.-Q. Shen, Chiral majorana hinge modes in superconducting dirac materials, Phys. Rev. B 103, L180504 (2021).
- [44] C.-H. Hsu, P. Stano, J. Klinovaja, and D. Loss, Majorana Kramers Pairs in Higher-Order Topological Insulators, Phys. Rev. Lett. 121, 196801 (2018).
- [45] Y.-J. Wu, J. Hou, Y.-M. Li, X.-W. Luo, X. Shi, and C. Zhang, In-Plane Zeeman-Field-Induced Majorana Corner and Hinge Modes in an s-Wave Superconductor Heterostructure, Phys. Rev. Lett. 124, 227001 (2020).
- [46] T. M. McCormick, I. Kimchi, and N. Trivedi, Minimal models for topological Weyl semimetals, Phys. Rev. B **95**, 075133 (2017).
- [47] T. Zhou, Y. Gao, and Z. D. Wang, Superconductivity in doped inversion-symmetric Weyl semimetals, Phys. Rev. B 93, 094517 (2016).
- [48] H. F. Yang, L. X. Yang, Z. K. Liu, Y. Sun, C. Chen, H. Peng, M. Schmidt, D. Prabhakaran, B. A. Bernevig, C. Felser, B. H. Yan, and Y. L. Chen, Topological Lifshitz transitions and Fermi arc manipulation in Weyl semimetal NbAs, Nat. Commun. 10, 3478 (2019).
- [49] E. Cheng, L. Yan, X. Shi, R. Lou, A. Fedorov, M. Behnami, J. Yuan, P. Yang, B. Wang, J.-G. Cheng, Y. Xu, Y. Xu, W. Xia, N. Pavlovskii, D. C. Peets, W. Zhao, Y. Wan, U. Burkhardt, Y. Guo, S. Li, C. Felser, W. Yang, and B. Büchner, Tunable positions of Weyl nodes via magnetism and pressure in the ferromagnetic Wevl semimetal CeAlSi, Nat. Commun. 15, 1467 (2024).
- [50] E. J. Sie, C. M. Nyby, C. D. Pemmaraju, S. J. Park. X. Shen, J. Yang, M. C. Hoffmann, B. K. Ofori-Okai, R. Li, A. H. Reid, S. Weathersby, E. Mannebach, N. Finney, D. Rhodes, D. Chenet, A. Antony, L. Balicas, J. Hone, T. P. Devereaux, T. F. Heinz, X. Wang, and A. M. Lindenberg, An ultrafast symmetry switch in a weyl semimetal, Nature **565**, 61 (2019).